The Aeronautical Journal (2025), **129**, pp. 1421–1444
doi:10.1017/aer.2025.6

RESEARCH ARTICLE

Hydrogen-air lean premixed turbulent highly swirled flames stabilisation: experimental demonstration and mechanistic-kinematic description

P. Palies[1,2] and C.P. Premchand[1,2]

[1]The Combustion and Propulsion for Aviation Research Center, The University of Tennessee Space Institute, Tullahoma, TN, USA
[2]Mechanical, Aeronautical and Biomedical Engineering Department, The University of Tennessee, Knoxville, TN, USA
Corresponding author: P. Palies; Email: ppalies@utk.edu

Received: 12 September 2024; **Revised:** 31 January 2025; **Accepted:** 4 February 2025

Abstract

Gaseous hydrogen chemically reacting with air in lean premixed mode yields essentially water vapour enabling to decarbonise aeronautical propulsion systems. When hydrogen fuel is produced by electrolysis, the impact on Earth is neutral on a life-cycle basis. Hydrogen fuel, combined to swirled premixed combustion mode, is a sustainable method for thermal-powered aviation. Knowledge gaps have hindered progress in the field and no laboratory-scale demonstrations have been made to date in the specific 100% H_2/Air swirled premixed regime. This study describes an experiment established to: (1) demonstrate this highly swirled lean fully premixed H_2/Air combustion mode and (2) -describe the underlying flame stabilisation principle. Theoretical results enable pioneering the first-to-date experimental stabilisation for these flames. Measurements with optical diagnostics including chemiluminescence and shadowgraphy direct imaging provide insights into the flame position and the flame regime. This experimental demonstration confirms that the kinematic balance between the flame displacement speed and the flow velocity is critical along with the flame-wall interaction at the bluff-body. It is shown that flashback can be mitigated. The present experiment can be replicated and utilised for application in several scientific disciplines and for advancing technologies. The experimental demonstration, regime characterisation method and mechanism description documented here open the perspective to deploy clean hydrogen combustion to decarbonise aviation with low nitrogen oxides emissions. The combination of high-swirl fully premixed H_2/Air experimental data and the theoretical results are unique.

Nomenclature

A_b	surface area at bluff-body [m^2]
A_α	flame angle tangent
A_{geo}	surface area at swirler [m^2]
d	injector outer diameter [m]
$\mathcal{L}_b$	Markstein length [m]
l_t	turbulence integral length scale [m]
Ka	Karlovitz number
Le	Lewis number
$\dot{m}_{air}$	air mass flow rate [kg s^{-1}]
$\dot{m}_{H_2}$	hydrogen mass flow rate [kg s^{-1}]
$\mathbf{n}$	flame front unit normal vector
Pe	Péclet number
S	swirl velocity ratio at the bluff-body
S_{geo}	swirler geometric swirl number

https://doi.org/10.1017/aer.2025.6 Published online by Cambridge University Press

$S_{geo,b}$	-geometric swirl number at the bluff-body
s_a	stoichiometric ratio
S_L^0	unstretched laminar flame speed [m s^{-1}]
S_L	stretched laminar flame speed [m s^{-1}]
S_d	local flame displacement speed [m s^{-1}]
T_b	burnt gas temperature [K]
T_u	unburnt gas temperature [K]
T^0	inner flame temperature [K]
U_b	mixture axial bulk velocity at the bluff-body [m s^{-1}]
u'	turbulent velocity fluctuation [m s^{-1}]
$v_{r,0}$	radial steady velocity component [m s^{-1}]
$v_{\theta,0}$	azimuthal steady velocity component [m s^{-1}]
$v_{z,0}$	Axial steady velocity component [m s^{-1}]
$\mathbf{v}$	Velocity vector at the flame front [m s^{-1}]
$\mathbf{w}_s$	flame front surface velocity vector [m s^{-1}]
Ze	Zeldovitch number

Greek symbol

α	base angle between vertical axis and flame front [deg]
β	local ratio of azimuthal flow speed to flame displacement speed
ε	mass flow rate reading uncertainty
η	Kolmogorov scale [m]
δ	flame thickness [m]
Δ_s	flame stabilisation criterion
κ	flame stretch [s^{-1}]
ϕ	equivalence ratio
μ	dynamic viscosity [Pa s]
ν	kinematic viscosity [m^2 s^{-1}]
ρ_b	burnt gas density [kg m^{-3}]
ρ_m	mixture reactant density [kg m^{-3}]
ρ_u	unburnt mixture gas density [kg m^{-3}]
τ_{cv}	through flame front convective characteristic time [s]
τ_b	burning characteristic time [s]

1.0 Introduction

The hydrogen economy has been proposed [1] to replace the fossil-fuel economy in order to address energy security, air quality and global warming. Towards this goal, hydrogen extraction and production methods, production site locations or transport modes and utilisation methods are critical. Among utilisation methods, there are two main foreseen paths: fuel-cells and thermal-powered technologies. The latter, based on the combustion of hydrogen fuel has been limited, with applications including rockets and ground-based gas turbines to date because of the following challenges: (i) safety concerns associated with autoignition, flashback, flammability and explosion limits, and minimum ignition energy, and (ii) generation of nitrogen oxides. The literature to date and the present study demonstrate that several of these challenges can be controlled, and the major identified flame stabilisation knowledge gap filled. Highly swirled hydrogen lean fully premixed flame associates a carbon-free fuel, a low adiabatic flame temperature reducing the thermal-induced nitrogen oxides formation occurring through the Zeldovich mechanism [2], and a highly swirled flow inducing an inner recirculation zone [3, 4] characterised by a reversal axial flow. This latter feature contributes ensuring scaling for a range of inlet air mass flow rates in combustors.

Flame stabilisation has been investigated in several studies for various combustion systems [5–7]. It can be defined as the branch of reacting fluid mechanics focused on understanding, describing and predicting flame position, shape and speed for thermal-powered applications. It also includes flashback

https://doi.org/10.1017/aer.2025.6 Published online by Cambridge University Press

[8] and blowout [9]. For swirling flames, a few major flow features are relevant to flame stabilisation or combustion dynamics. Among the known features for swirling flows are: the vortex breakdown [10, 11] either axisymmetric or spiral, the characteristic flow shear layers [12], the inner recirculation zone resulting from the vortex breakdown [3], and the global spiral mode also referred as helical mode documented in literature [13]. The vortex breakdown [11] occurs when the ratio of tangential momentum flux to axial momentum flux, most often defined with a swirl number or swirl to axial velocities ratio, reaches a critical value. This induces a flowfield change charactersed by a stagnation point followed by a reversal velocity region: the inner recirculation zone. Low swirl flames do not have this feature whereas highly swirled flames do. This zone is used in gas turbine combustors to anchor swirling flames. To date understanding is highly swirled flame are stabilised because this reverse flow has a favourable low speed region of hot burnt gases continuously igniting the upstream fresh mixture. A precessing vortex core [14, 15] (PVC) can be superimposed on the inner recirculation zone (IRZ) induced by the axisymmetric vortex breakdown and both the PVC and IRZ can exhibit precessing motions of the vortex core and of the stagnation point, respectively.

Whereas flame stabilisation processes have been studied for low swirl flames at atmospheric conditions and at high swirl for several fuels blended with hydrogen, there is no prior research for the high swirl 100% hydrogen-air premixed fully regime because of flashback [16] and no general stabilisation criterion available for these flames. The present experimental and analytical research leads to a criterion for lean fully premixed highly swirled flames in the near unity Karlovitz number turbulent premixed combustion regime. In this regime, referred to the flamelet regime [17, 18], the local flame displacement speed is the so-called stretched laminar flame displacement speed S_L [19–21]. This quantity has been classically measured with the spherical expanding flame configuration for hydrogen/air premixed flames in several studies [22, 23]. Lean premixed hydrogen-air flames can exhibit cellular structures on the flame front surface associated to preferential diffusion [24–26]. When swirl is added, competing effects between the cellular structures and the swirler-induced turbulence impact the flame sheet wrinkling. Whereas those effects are yet to be delineated in highly swirled configurations, literature to-date [25, 27–29] indicates that the flame front remains in the flamelet or corrugated regime where the stretched laminar flame displacement speed is relevant, yet with significant variations across the flame surface.

Von Elbe and Lewis [30] documented initial work on laminar premixed flames with the development of a theory for stabilisation based on the representation of the flame front as a single surface inclined at a given angle with respect to the unburned premixed stream. The flashback of this flame front was shown to be controlled by thermal quenching on the rim of the burner by comparing theoretical results with experimental data. Cheng *et al.* [31] researched turbulent low swirled premixed flames. To stabilise the turbulent premixed flame fixed in the laboratory frame of reference, the low-swirl burner [32] (or injector) employs a flow that lower the swirl level so that vortex breakdown, a precursor to the formation of flow reversal and recirculation zone, does not occur, yielding a different flowfield and flow regime than high swirl. Those pioneering studies [30, 32] emphasised respectively the role of the laminar flame displacement speed S_L^0 and the turbulent flame speed, versus the local flow speed in flame stabilisation, and thus the link to kinematic. Demonstrations of turbulent highly swirled fully premixed methane/air flames have been made by Williams *et al.* [33], Thumuluru and Lieuwen [34] and Palies *et al.* [35]. In the former study [33], the operating envelope of the combustor was experimentally assessed to map region of combustion instabilities, blowout and stabilised flame. All near flame components were water-cooled in this system. In Refs. (34, 35) the focus was on flame response measurements. Low swirled flames with mixture of blended H_2-CH_4-Air gases have been investigated by Davis *et al.* [36], Therkelsen *et al.* [37] and Palies *et al.* [38] with respect to thermoacoustic instability. These studies pioneered H_2-CH_4-Air low swirl flames and demonstrated that both low swirled and high swirled flames obey to identical combustion instabilities mechanisms.

The turbulent highly swirled premixed flame regime with hydrogen enrichment of methane-air premixtures have been investigated by Schefer *et al.* [39] and Burguburu *et al.* [40] initially. The addition of hydrogen to a premixture of methane-air in low swirl flames [37] was shown to change the flame

https://doi.org/10.1017/aer.2025.6 Published online by Cambridge University Press

shape significantly, an observation also reported for highly swirled flames [39]. The investigation of two injections strategies (partially premixed versus fully premixed enrichment of aviation jet fuel) in Ref. [40] showed that the partially premixed regime yields higher nitrogen oxides that can be attributed to the occurrence of regions of both lean and richer mixtures compared to the fully premixed case. The study of Taamallah *et al.* [41] focused on the effects of the CH_4 to H_2 mass fraction ratio of the premixture, flow Reynolds number, swirler blade angle and heat loss with respect to the presence or not of the outer flame branch. The authors [41] proposed that the flame transition from inner only branch to inner/outer branches was driven by a flow and flame times associated respectively with an unsteady process on the outer branch and an extinction strain rate characteristic time. Guiberti *et al.* [42] investigated high swirl for H_2-CH_4-Air mixture with particular attention to the combustor's wall heat transfer. This heat transfer was shown to induce either a flame stabilised with an inner only or both an inner plus outer branches. Chterev and Boxx [43] conducted experiments to observe the flame shape at various operating pressures (1, 3 and 5 atm) up to 50% hydrogen content in volume of the fuel blend. Experiments were complemented with computational studies by Agostinelli *et al.* [44] for stabilisation understanding in the partially premixed regime. It was experimentally shown [43] that a flame with both inner and outer branches stabilised at atmospheric pressure for low hydrogen enrichment content. When increasing the hydrogen content, a transition was shown towards a flame stabilised with only the inner branch depending upon the hydrodynamic strain in the shear layer. Both regimes were observed in between low and high hydrogen content cases. It was also concluded that increasing both operating pressure and hydrogen enrichment decreased the flame length. Highly swirled flames in the partially premixed flame regime has been studied in a configuration without center-body by Reichel *et al.* [45, 46] with preheated inlet air. Sattelmayer *et al.* [47] and Mayer *et al.* [48] investigated technically premixed hydrogen-air swirled flames stabilisation and flashback mechanisms with preheated air. In these configurations, the fuel is injected respectively through multiple holes [45] or tangential slits [48, 47] to mix with air without a premixing unit as undertaken in this article. The turbulent low swirled regime with 100% hydrogen content was pioneered by Cheng *et al.* [32]. The study [32] demonstrated a similar stabilisation mechanism both at atmospheric and gas turbine operating conditions.

The blowout, also known as flameout occurring when a flame exits the combustor, and the blowoff occurring when a flame extinguishes on itself in the lean flammability limit are also important processes relevant to flame stabilisation. Both mechanisms can occur together for premixed flames [49]. For swirling flames in the fully premixed mode, this phenomenon arises mostly at the lowest equivalence ratios near the lean flammability limit. A few articles have investigated the transient to blowoff/blowout and the underlying mechanisms in fully premixed regime. For bluff-body flames, the mechanisms have been established as a sequence of three steps [9]. During the first step, local extinctions occur on the flame front, whereas in a second step, large scale features are at work and ultimately lead to blowoff onset, the last step. This onset is due to the inner recirculation zone cooling and its size reduction. The effect of turbulence has also been researched [50] with the observation of a broken reaction zone prior the blowoff onset. Experimental velocity measurements confirmed the reactants motion towards the recirculation zone. This process has been investigated on swirled premixed flames as well recently [51] with laser diagnostics and analyses. Identification of extinction events on the flame sheet were associated with the likelihood of unburnt mixture flowing throughout the subsequent flame holes [51] caused by local extinction. In Ref. [49], computations were conducted to describe the mechanisms of transition to lean blowout initially observed on the experiment of Cavaliere *et al.* [52]. Whereas extinction events were not observed on the flame sheet, the simulations demonstrated the entrainment of unburnt premixture towards the inner recirculation zone. Limited work to date has been undertaken for premixed hydrogen-air swirled flames to confirm those mechanisms.

The flashback of premixed highly swirled flames has been the topic of several works. Fully premixed methane and H_2-CH_4 blend [53, 54] flames have been studied to describe basic mechanistic behaviour with advanced high-speed particle image velocimetry and chemiluminescence flame imaging. Transient sequences of flame flashing back in the upstream tube demonstrated the existence of large-scale flow feature creating a local negative axial velocity sustaining the upstream propagation. These works

https://doi.org/10.1017/aer.2025.6 Published online by Cambridge University Press

also support a kinematic flow-flame front description. Research on flashback with 100% H_2/Air highly swirled flames have been made as well [16, 55] with emphasis on the boundary-layer flashback process and the derivation of correlation based on the axial non-reacting velocity of the mixture upstream the flame.

The goals of this article are to describe an experiment enabling stabilisation of 100% H_2/Air highly swirled fully premixed flames along with theoretical development to form a general stabilisation map for these flames. After the introduction of the state of the art, the first section of the paper describes the experiment and the methodology. The second section presents the detailed burner geometry and the operating conditions. The third section documents the experimental measurements. The fourth section discusses the flame stabilisation criterion theory. The last section compares the analytically derived stabilisation map with the experimental data. The conclusion summarises the main outcomes of the paper and provides scaling considerations.

2.0 Laboratory scale experimental setup description

The laboratory scale experimental setup is depicted in this section. Four key components are described: the fuel storage and dispensing unit, the premixing unit, the burner unit (defined as 'the experiment'), and the exhaust unit. The experiment is an evolution of the premixed swirled flame experiment documented in Ref. (35).

The fuel storage and dispensing units are now described. High-pressure 350 bar cylinders of hydrogen (industrial-grade hydrogen, size 200 high-pressure steel cylinder, CGA 350), methane and nitrogen gases are stored into a vented cabinet located outside of the laboratory. A pipe connects one of the selected cylinders to the experiment in the lab. A relief valve is located outside the laboratory on that gas line. Nitrogen is used to purge fuel from the gas line after each experimental campaign. Both hard (stainless steel) and flexible gas pipes are employed for the flows of hydrogen, nitrogen, air (onsite compressed air) gases and water used for burner's cooling. Ball valves, regulators, pressure gauges and check valves are utilised on the air and fuel lines. The fuel and air mass flow rates are measured and controlled through Labview. Omega flow rate controllers' devices are utilised of respectively 500 SLPM (model FMA-2612A) and 2000 SLPM (model FMA-2622A) maximum volumetric flow rates. The instruments reading error ($\pm 0.8\%$) and full-scale error ($\pm 0.2\%$) are discussed in Section 4. The corresponding fuel and air lines are connected to the inlet of the premixing unit described next.

The premixing unit consists of a cylinder part with two inlets: one for the fuel (methane or hydrogen) and one for the air on its upstream side; and two outlets on its downstream side where the resulting premixture exits. Schematic and photos are displayed in Fig. 1. This premixing unit consists of a 40 cm in length and 22 mm diameter metal cylinder with a coaxial central rod. On this rod, coaxially to the outer cylinder, a series of four successive, fixed and evenly distributed co-rotating directions swirlers are mounted to mix the air and the fuel. At the two outlets of the outer cylinder, flexible gas pipes connect the formed premixture to the burner base. For the present study, only one gas pipe is necessary. This pipe is equipped with two commercial inline flame flashback arresters.

Schematic and photos of the experiment are shown in Fig. 2. The premixed flow passes through a perforated plate positioned at the base of the burner to mitigate large-scale turbulence.

The mixture is then convected in the converging unit (water-cooled component) where the flow is accelerated. A set of O-rings are used to seal joints between separate parts and prevent leaking of gases. The mixture next passes through a flame arrester made of three layers of stainless steel of five micrometer opening size, which is below the Kolmogorov scale in the present study. This flame arrester sizing was selected based on the model by Hong and Song [56] applied to hydrogen and air mixtures. A conservative choice was made for safety purpose. The premixture is then set into rotation by the swirler. The swirler is made of eight blades based on NACA 8411 twisted profiles. The cylindrical clear fused quartz tube allows optical access (70 mm inner diameter and 100 mm in length), and it is situated on the backplane of the burner. A bluff-body is tied at the top of the central rod where the flames are stabilised. The water flow rate in the cooled converging unit and the central rod is set to one gallon per minute (minimum

https://doi.org/10.1017/aer.2025.6 Published online by Cambridge University Press

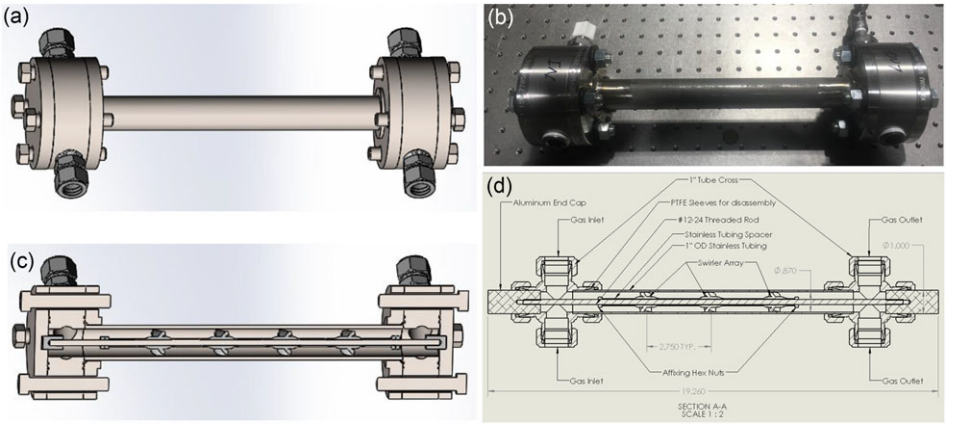

Figure 1. *Premixing unit. (a) 3D schematic with separate air and fuel inlets on the left and the two premixture outlets on the right. (b) Photography. (c) Cutaway enabling to visualise the four successive swirlers inducing the mixing. (d) Detailed schematic (version with three swirlers shown).*

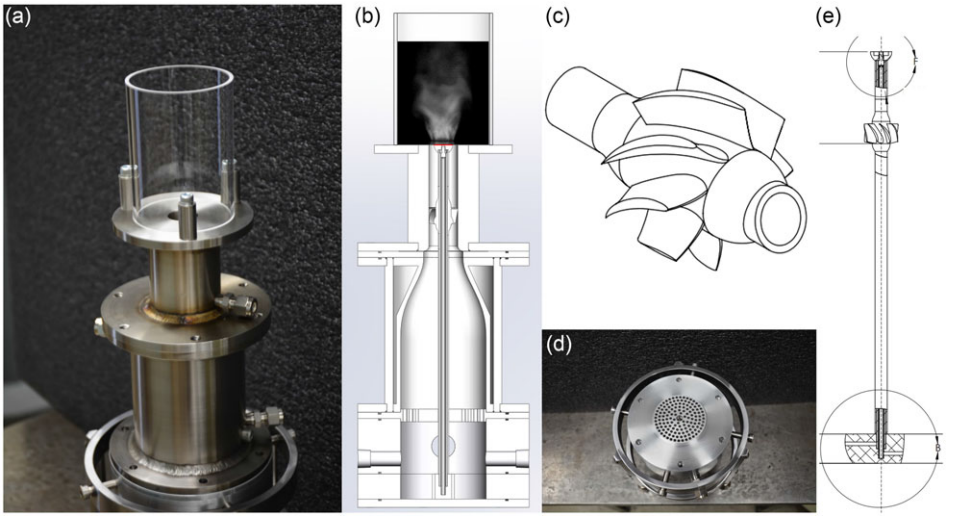

Figure 2. *Experimental setup components. (a) Photo of the semi-assembled burner. (b) Schematic with the red line indicating the 13.6 mm bluff-body diameter. (c) Swirler. (d) Perforated plate. (e) Water-cooled rod equipped with an unfilled, unflushed bluff-body.*

flow rate) and measured with a clear-in line panel mount flow Omega meter device with an uncertainty of ±5% full scale.

The experiment can be setup for methane-air or hydrogen-air fully premixed flames with or without swirler for several bluff-body shapes and diameters as well as two central rod diameters. In this article, a single bluff-body model is utilised: the filled baseline shape of 13.6 mm diameter which shape is shown in both Figs. 2(b) and A1(b) in Appendix B. The present bluff-body is flush- with the backplane of the combustor, green coloured in Fig. 3(c). Initial non-reacting numerical simulations of the experiment equipped with identical geometry (swirler and baseline bluff-body) without perforated plate nor flame arrester have shown the formation of a strong inner recirculation zone [57].

The swirler part drives the flow rotation. It has eight blades periodically spaced around the central rod. The trailing edge pressure side blade angle with respect to the vertical is non-constant. A radial

https://doi.org/10.1017/aer.2025.6 Published online by Cambridge University Press

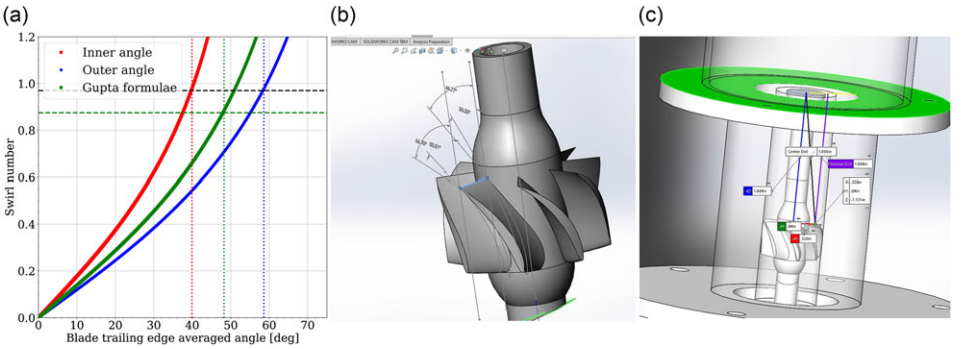

Figure 3. *(a) Swirl number curves. (b) Swirler geometry with angles at the trailing edges shown on both sides of the blade. (c) Swirler blade trailing edges are located 47 mm upstream of the injector backplane (green-coloured surface).*

dependent profile for the angle between the inner diameter (hub) and the outer diameter (tip) is used. Taking into account this radial evolution of the angle, chapter 1 of Ref. (58), and the classical Gupta formulae [4] for swirl number calculations, an averaged geometrical swirl number from both formulae is determined. One obtains $S_{geo} = 0.92$, see Fig. 3(a).

As the mixture evolves downstream along the cylindrical component and reaches the bluff-body, the flow surface area reduces due to the bluff-body diameter larger than the swirler inner diameter. It induces a swirl number reduction as shown in Appendix C of Ref. (58). This change can be estimated as follows:

$$S_{geo,b} = S_{geo} A_b^2 / A_{geo}^2 \tag{1}$$

and the numerical value is 0.68 at the bluff-body tip.

Experiments were first conducted to assess the flame arresters capability to stop flashback on a modified Bunsen burner, see Fig. 4, where the characteristic cylindrical metal component of the burner was made optically accessible. In addition, a ring was added at mid-height of this cylindrical component to hold a flame arrester sample. It allowed to test multiple flame arrester materials and their opening sizes. Those tests led to select a commercially available mesh made of a five-micron twill dutch weave stainless steel screen opening size (T316 micronic stainless UNS S31603 with wire diameters of 0.0508 and of 0.03048 mm). This mesh meets the standard specification ASTM E2814-18. The thickness is 0.1118 mm and the surface density is 0.78 kg m^{-2}. Both methane/air and hydrogen/air flames flashing back were tested. Flashback was triggered by reducing the mixture bulk flow rate from the stabilised points.

The experiment and measurement diagnostics are located under an exhaust unit made of a hood connected to an approximately 15 meters, 10-inch diameter pipe ended by an extracting fan (rated at 1275 SCFM) for the extraction of gases of multiple experiments. A level of 450 SCFM at the exhaust duct above the present experiment was measured at maximum fan speed for the present setup. Two sensors (model HIC 822, Indtl. Test Equipment) are used to detect any accumulation of hydrogen fuel. It is calibrated to alarm at 200 ppm of hydrogen content (0.5% of low explosive limit). One sensor is mounted inside the exhaust hood whereas the other one is located outside, near the fuel valve. The experiment is installed on an optics table. Four panels allow to operate the experiment in an enclosure between the optics table and the exhaust hood. The shadowgraphs were obtained with two panels opened whereas chemiluminescence data were obtained with all panels closed. The exhaust gas hood was specifically designed to cover all major components located underneath and to direct all burnt gases outside. The approximate dimensions of the hood are 4 ft. in length, 2 ft. in width and 1 ft. in height. The exhaust fan has a maximum continuous temperature of 450 K which is expected to be higher than the temperature reached by the burnt gas mixed with ambient air at that location.

https://doi.org/10.1017/aer.2025.6 Published online by Cambridge University Press

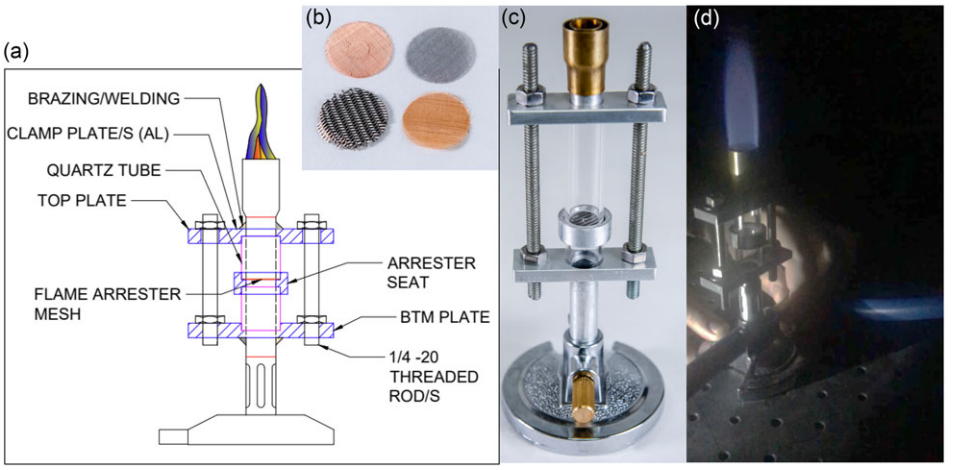

Figure 4. *Modified Bunsen burner for flame arresters assessment. (a) Schematic. (b) Samples of flame arresters made of different materials and opening sizes. (c) Photo of the modified Bunsen burner prior operation. The ring that holds the flame arrester sample is seen. (d) Photo of the system operating (CH_4/Air) prior to flashback.*

The ignition and subsequent stabilisation of highly swirled flames presented in this article have been made through an increasing level of complexity and verification steps. Firstly, conical diffusion flames were ignited and stabilised on the Bunsen burner. Next, this burner was modified to be directly connected to the premixing unit described above. This allowed to control precisely the equivalence ratio and to operate the modified Bunsen burner in fully premixed mode. Ignitions were then triggered on ultra-lean equivalence ratio mixtures (equivalence ratio $\phi = 0.3$) at low bulk velocity (near or below 2 m s^{-1}) successfully. A parametric study for equivalence ratio and bulk velocities demonstrated smooth ignition for low values of both parameters. Secondly, the swirl experiment documented in this article was utilised without the swirler to demonstrate both smooth ignition of 'V' flames and stabilisation. In both the Bunsen and swirl burners, methane fuel was used to test the setup prior to use hydrogen. During those series of tests of increasing level of complexity, a robust approach for ignition, flame arrester assessment and operation were made. The ignition was triggered with a commercial lighter (brand name VEHHE) based on plasma flameless arc technology.

3.0 Geometry and operating conditions

The geometry of the experiment described in the above section is depicted in Fig. 5(a,b). All major elements of the burner are sketched. The operating conditions are given in the unstretched laminar flame speed S_L^0 map of Fig. 5(c) where the H_2/Air mixture equivalence ratio ϕ ranges from 0.3 to 1 along the x-axis and the bulk mixture axial velocity at the bluff-body U_b ranges from 0 to 14 m s^{-1} along y-axis. The bulk flow velocity remained below 7.5 m s^{-1} to limit the thermal power of the undertaken set of experiments. Experiments were conducted for thermal power ranging from 0.46 kW (equivalence ratio 0.3 and bulk mixture velocity of 1.7 m s^{-1}) to 3.1 kW (equivalence ratio of 0.5 and bulk mixture velocity of 7.41 m s^{-1}). The thermal power is defined as $P_{th} = \dot{m}_f \Delta h$ where $\dot{m}_f$ is the fuel flow rate and Δh is the energy released by combustion of hydrogen fuel and is equal to 120 MJ kg^{-1} (lower heating value). Higher thermal powers were not tested to avoid overheating of the burner as well as allow safe operations within the current laboratory settings.

Each coloured symbols on the map of Fig. 5(c) represents a measurement point. Superimposed to the map are: Karlovitz number isovalue lines for levels of 0.01, 0.25, 1 and 7; Lewis number isovalue lines for levels 0.45 and 0.55; as well as Kolmogorov scales values of 60, 90 and 180 micrometers.

https://doi.org/10.1017/aer.2025.6 Published online by Cambridge University Press

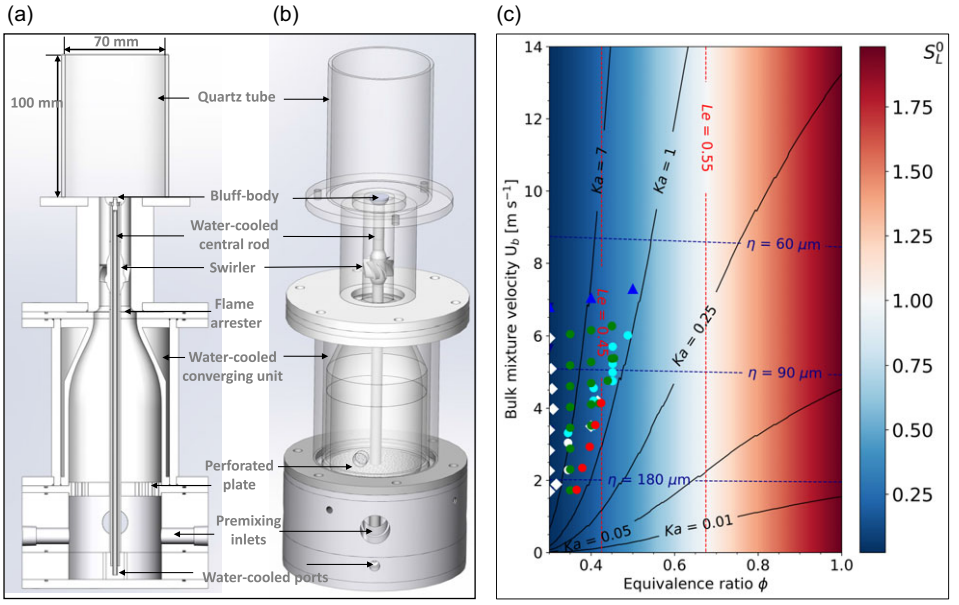

Figure 5. *Geometry and operating conditions map of the experiment. Cutaway (a) and isometric view (b) of burner unit. The swirler, the bluff-body, the water-cooled converging unit and the central rod are shown. Operating conditions map (c) of the experiment with Kolmogorov scales, Lewis and Karlovitz numbers isolines superimposed on the unstretched laminar flame displacement speed S_L^0 (m s^{-1}) contour. Symbols represent experimentally assessed points on the operating conditions map: whites squares are ignition points, green dots are stabilised flames, red dots are flashback data points, cyan dots are additional stabilised data points and blue triangles are stabilised points that include high-speed transient sequences.*

The values for all isolines superimposed on the flame operating conditions map were selected to include representative's levels across their entire respective ranges (evenly distributed spatially). The white symbols correspond to ignition points, green dots correspond to stabilised flames, red dots to flashback points, cyan dots to additional stabilised points and blue triangles-up to stabilised points that include high-speed transient sequences. The symbols and their colour indicate different experimental campaign. Fig. 5(a–c) comprehensively characterises the geometry of the experiment and the operating conditions of this study. This setup, the measurement techniques, the operating conditions and the experimental procedure are described in the next sections.

The operating condition map parameters depicted in Fig. 5(c) are defined now. The Kolmogorov scale is defined with:

$$\eta = l_t \left(\frac{\rho_m u' l_t}{\mu} \right)^{-3/4} \tag{2}$$

The turbulence integral length scale is taken as $l_t = 0.9\ d$ where d is the injector outer diameter (22 mm) in the present study. The turbulent velocity fluctuation is $u' = 0.2\ U_b$. The factor 0.2 is an estimate deduced from a scaling reported and used in previous works [29, 49, 59]. The mixture density ρ_m and its dynamic viscosity μ are obtained from the open-source software cantera [60]. The Karlovitz number defined as $\mathrm{Ka} = (\delta/\eta)^2$ is used to generate the isolines values in Fig. 5(c) where δ is the thermal diffusive flame thickness. The Lewis number is computed as $\mathrm{Le} = \mathrm{D}_T/\mathrm{D}_{H_2}$. The thermal diffusion coefficients D_T, the mixture-averaged diffusion coefficient for hydrogen D_{H_2}, the unstretched laminar flame speeds S_L^0, the species binary diffusion coefficients used to compute D_{H_2}, and the composition data are obtained

https://doi.org/10.1017/aer.2025.6 Published online by Cambridge University Press

from cantera one-dimensional flame simulations. Those calculations are based on the state of the art [61, 29, 49].

4.0 Measurement techniques and experimental results

In this section, the experimental measurement techniques and the results obtained are described. The measurement techniques used for the visualisation of the flame for all operating conditions and the geometry include: (i) chemiluminescence imaging, and (ii) shadowgraph imaging. The chemiluminescence flame imaging technique is used to capture the flame front position (time-averaged and transient evolution). The flame position data inform subsequently on the flame stabilisation. The shadowgraph imaging technique is used to capture the flame location as well. It especially informs on the presence of inner or inner/outer branches. Images of spatial distribution of flame light emissions for the H_2/Air premixed flames are obtained using a high-speed camera that captures ultraviolet (UV), visible light and near IR wavelengths, a key enabler for hydrogen-air flames. A high-speed Phantom T2410UV-VIS monochrome camera capturing wavelengths ranging from 200 nm to 1100 nm is utilised. The camera is equipped with a CMOS back side illuminated sensor with fused silica and a global shutter. Based on the manufacturer camera's spectral response, at 308 nm (which corresponds to OH^* flame emission), the quantum efficiency of the camera is superior to 70%. The maximum resolution is 1280 by 800 pixels at 24,270 frames per second (fps) with a minimum exposure time of one microsecond. The maximum frame rate is 558,330 fps on a reduced window size of 1280 by 32 pixels.

Two F-mounted lenses are utilised with the camera: a Nikon 50 mm F/1.8 E for chemiluminescence imaging and a Tokina AT-X SD 300 mm F/2.8 MF for shadowgraph. A Fotodiox macro extension tube set (Nikon F-mounts for both camera body and lens sides) is employed to increase the spatial resolution (defined as the number of pixels per millimeters of field of view) for chemiluminescence imaging. The tube employed consists of the mount body and mount lens part only that corresponds to a 15 mm extension tube. All flame electromagnetic waves radiations emitted (UV or not) are directly collected on the high-speed camera CMOS sensor.

The shadowgraph optical arrangement is now described. A 150W Halogen bulb light source is connected to an optic fiber. This fiber is placed upstream of a condenser lens (Edmund optics 50 mm diameter and 44 mm focal length) converging the non-monochromatic light onto a slit acting as the point source of the optical system. This light source is then transmitted to the first parabolic mirror (25 cm in diameter), crosses the flame, and reflects on the second mirror. The light is then collected on the Tokina 300 mm focal lens optic to capture the transient flame data that are recorded as *.cine* files in the PCC software and post-processed with the SDK13.8.804 suite of tools.

It is worth pointing out that the time-averaged fields obtained are slightly dissymmetric because of (i) location of the swirler blades with respect to the field of view of the camera, (ii) slight deviation of concentricity between central rod and burner injector and (iii) non-spatial averaging of data. Variance fields are computed as the average of the squared differences between each time instant value with the mean value.

Inverse Abel transforms were applied to the chemiluminescence images. This mathematical transformation takes a line-of-sight integrated time-averaged chemiluminescence image and reconstructs it as a slice through the three-dimensional distribution. This corresponds to (d_2, e_2, f_2) panels in Fig. 8. The algorithm implementation by Hickstein *et al.* is used [62] in the present study.

The spatial and temporal resolutions for both measurement techniques are now discussed. For the chemiluminescence imaging, the high-speed camera was operated at 1000 fps. The exposure time was set to 990 microseconds to maximise photons collection. The characteristic time associated with the flame front propagation at an equivalence ratio of 0.4 is below one millisecond. In the present case, the exposure time is nearly equal to the flame burning propagation time. This characteristic time was determined as the ratio of the flame thickness to the flame displacement speed ($\tau = \delta/S_L^0$). For an equivalence ratio of 0.4, the thermal diffusive flame thickness is 0.174 mm and the laminar unstretched flame speed is 0.176 m s^{-1} (making use of Conaire *et al.* [63]). This yields a characteristic time of 0.98 ms. In other

https://doi.org/10.1017/aer.2025.6 Published online by Cambridge University Press

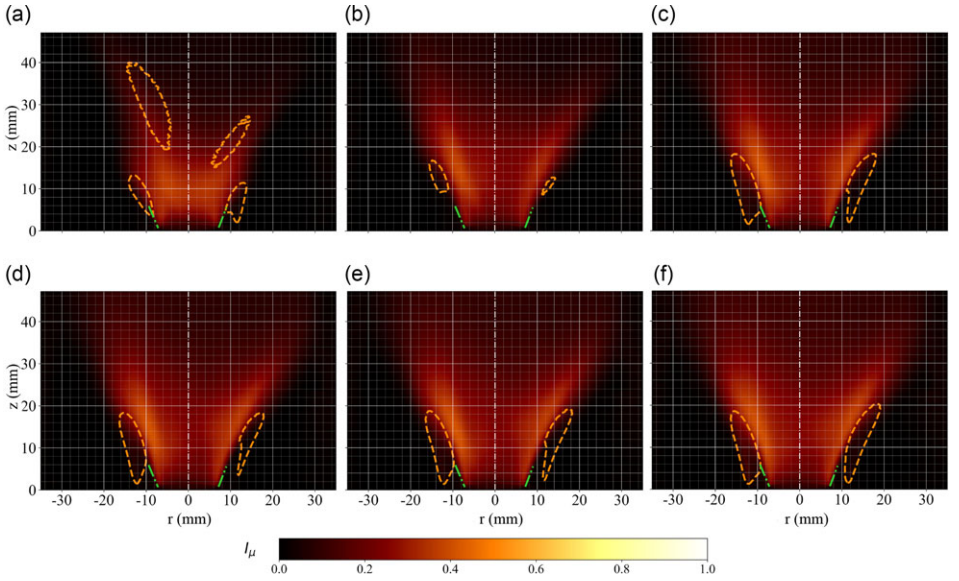

Figure 6. *Time-averaged flame images at constant equivalence ratio 0.3 for several increasing mixture velocities from 1.7 m s^{-1} (a) to 6.79 m s^{-1} (f).*

words, during the acquisition, the flame propagation due to burning is essentially occurring over a distance equals to the flame thickness. When considering the flame surface velocity vector $\mathbf{w}_s$, additional blurring effects are at stake as the flame front propagates over larger zones due to convective transport of the flame surface. This selected setting allows to record sufficient signal for each frame in this lean regime that is known as a low light regime, especially for hydrogen flames. It does not avoid blurring effect of the flame front. Shorter exposure times and higher fuel flow rates will be required for instantaneous descriptions based on chemiluminescence data. The field of view is a rectangle window of 75.3 mm (1280 pix) by 47 mm (800 pix) and the corresponding spatial resolution is 17 pixels per mm. As the thermal diffusive flame thickness is 174 micrometers at an equivalence ratio of 0.4, this corresponds to three pixels per flame thickness. Graph sheets are used to set the field of view and determine the spatial resolution. Prior each experimental video acquisition, a photo was taken for background subtraction on the subsequent transient sequence. For the shadowgraph transient sequences, the camera acquisition rate is set to 35 000 fps and the exposure time to one microsecond. The field of view is 71.2 mm (768 pix) by 47.4 mm (512 pix) corresponding to 10.7 pixels per millimeters. An object of known size is used to determine the spatial resolution.

The optimal frame rate and exposure time result from the balance between capturing sufficient light to determine the flame position for a given flow condition and avoiding blurring effect. As the equivalence ratio is reduced, the intensity from chemiluminescence naturally reduces. In addition, at a given equivalence ratio, the reduction or increase of mixture velocity respectively reduces or increases the intensity because the fuel flow rate changes. This effect is shown with the time-averaged fields shown in Fig. 6 with corresponding integrated light signals in Fig. 7. For the present research, the methodology consisted of selecting the shortest exposure time possible at the highest frame rate per second (fps). Above 1000 fps, the exposure time was too short and thus the flame was not well seen. Below 1000 fps, the blurring effects were too strong, and the flame appears fully laminar or the camera sensor saturated because of too strong flame emission's signal. Higher frames rates can be obtained if brightness, gamma, and tone settings are changed or the signals intensities post-processed. In this article, no modifications, either in the camera software or a posteriori, are made to the signals measured.

https://doi.org/10.1017/aer.2025.6 Published online by Cambridge University Press

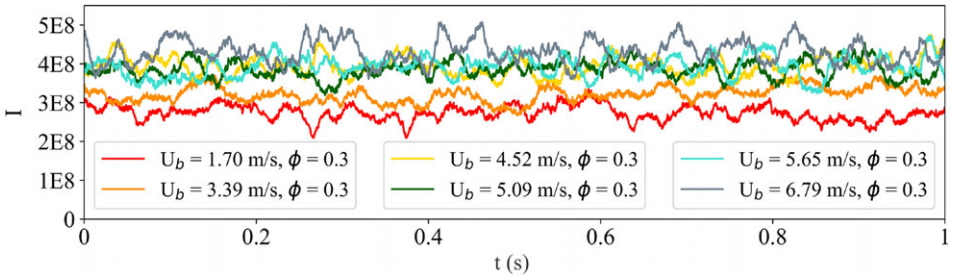

Figure 7. *Timeseries of integrated chemiluminescence signals at constant 0.3 equivalence ratio for several increasing mixture velocities from 1.7 m s^{-1} (a) to 6.79 m s^{-1} (f).*

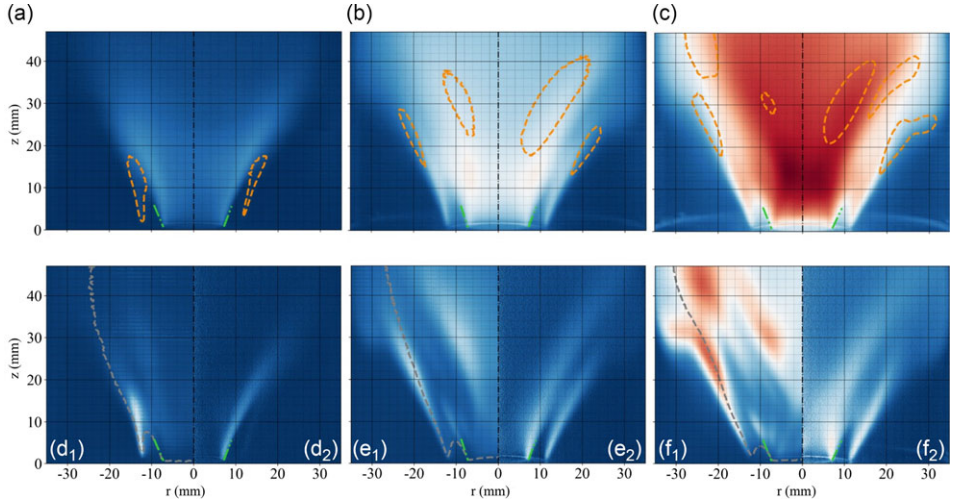

Figure 8. *Experimental flame imaging for equivalence ratio 0.3, 0.4 and 0.5 from left to right at constant air bulk velocity 6 m s^{-1}. Measured time-averaged chemiluminescence emission fields are shown on panels (a, b, c) with constant variance isolines (orange dashed line) overlaid. Chemiluminescence emission variance fields are shown in panels (d_1,e_1,f_1) with superimposed time-averaged contours (grey dashed line). Inverse Abel transform of the time-averaged fields are shown in panels (d_2,e_2,f_2). Data are scaled by maxima taken at the highest equivalence ratio.*

The uncertainty for the mass flow rate controllers includes the reading error plus the full-scale error. The full-scale error (±0.2% of full scale value), includes errors from: calibration, vibration and mechanical stress impacting the sensor accuracy, drift in accuracy over time, moisture level, flow direction and turbulence conditions at each test. In practice, for the present experiment all those contributions are low because the instruments are new and calibrated so without drift due to time. Also, these devices are utilised in an air-conditioned room (level of moisture and ambient conditions similar) and for a range of similar flow speeds between experiments. In addition, the instruments are not subject to mechanical vibrations or stress (they are attached to the optic table). Accordingly, the full-scale error was neglected for the present experimental dataset.

The uncertainty ε is ±0.8% of reading for fuel and air mass flow rates controller and is considered now. This uncertainty is assessed for both the equivalence ratio and the bulk flow mixture velocity, corresponding to x-axis and y-axis respectively of Fig. 5(c), with a method described next. The equivalence ratio ϕ is defined as the ratio of hydrogen and air mass flow rates of the mixture to the same quantity at the overall chemical reaction stoichiometry for hydrogen-air:

https://doi.org/10.1017/aer.2025.6 Published online by Cambridge University Press

$$\phi = \frac{\dot{m}_{H_2}/\dot{m}_{air}}{(\dot{m}_{H_2}/\dot{m}_{air})_{stoichio}} \tag{3}$$

The denominator is referred to s_a, the stoichiometric ratio which is equal to 0.029 for hydrogen-air. Maximum and minimum values of the equivalence ratio are obtained as a function of the manufacturer uncertainty ε. This yields to a minimum value ϕ_{min} for a given equivalence ratio ϕ defined with:

$$\phi_{min} = \phi \frac{1-\varepsilon}{1+\varepsilon} \tag{4}$$

And for the maximum value ϕ_{max}:

$$\phi_{max} = \phi \frac{1+\varepsilon}{1-\varepsilon} \tag{5}$$

The calculation of the uncertainty range corresponding to those two expressions was conducted and shown to be of low amplitude. For an equivalence ratio ϕ of 0.4, the range is ± 0.006. An identical method to determine the uncertainty range was used for the bulk mixture velocity quantity, y-axis of Fig. 5(c). The corresponding expression for the minimum bulk mixture velocity is:

$$U_{b,min} = \dot{m}_{air}\,(1-\varepsilon)\,(1+s_{air}\phi_{min})\,/\rho_m A_b \tag{6}$$

Where ρ_m is the density of the premixture and A the section area where the bulk velocity is calculated (at the bluff-body tip in the present study). For the maximum value $U_{b,max}$ the expression is:

$$U_{b,max} = \dot{m}_{air}\,(1+\varepsilon)\,(1+s_{air}\phi_{max})\,/\rho_m A_b \tag{7}$$

For an equivalence ratio ϕ of 0.4 and a bulk mixture velocity of 7.16 m s^{-1}, the range is -0.06 and $+0.06$ m s^{-1}.

The experimental results documented in this study were repeated several times (between two to ten times, one for flashback data points) on different days at different times.

Results corresponding to blue triangles-up in Fig. 5(c) are now discussed. Those points correspond to constant air flow rate and increasing hydrogen mass flow rate up to 3.1 kW thermal power, the maximum of this dataset. Data shown in Fig. 8 were obtained with axial bulk mixture velocity of 6.9 m s^{-1}, 7.16 m s^{-1}, and 7.41 m s^{-1}. For these three cases, the corresponding axial bulk air flow velocity is 6 m s^{-1}. The axial bulk mixture velocity is increased due to the equivalence ratio increasing from 0.3 to 0.5.

Direct flame chemiluminescence imaging results are shown in Fig. 6 (top and central rows) along with instantaneous shadowgraphs (bottom row). Each column corresponds to one equivalence ratio, respectively 0.3, 0.4 and 0.5 from left to right at constant air bulk velocity 6 m s^{-1}. Multiple observations can be made from Fig. 6. First, full premixed hydrogen-air swirling flames can be stabilised, and flashback avoided. This is shown both with the presence of the quartz tube for the chemiluminescence technique and without it for the shadowgraph. This is a central result of this study. Secondly, the flame shape evolves from a 'V' shape (inner branch only) at low equivalence ratio of 0.3 to a 'M' flame shape (inner plus outer branches) at 0.5. In the former, the chemical reactions sustaining the premixed flame front propagation are located on a single branch located at the interface of the swirling jet and the inner recirculation zone. In the latter, those are also located between the swirling jet and the outer recirculation zone located above the backplane and near the quartz tube when present. The transition of premixed flame shape has been documented in several articles with identified effects from the flame stretch [64], the precessing vortex core [65], the heat loss [42] or the outer rim flow/flame scales [41, 66]. The inner branch is always present for a swirler plus bluff-body configuration whereas for the outer branch, it is not always the case.

Post-processed estimates indicate an averaged 21 degrees flame angle as defined between the vertical axis and the inner time-averaged flame branch. This value holds across equivalence ratios at constant inlet air bulk velocity. A green dashed line marking the angle at the base of the flame front is shown on each panel. The emitted light signal intensity naturally increases as the equivalence ratio rises from 0.3 to 0.5 as more photons resulting from chemical reactions are released. A similar observation holds at constant equivalence ratio and increasing inlet air velocity as previously discussed. Whereas the mean

https://doi.org/10.1017/aer.2025.6 Published online by Cambridge University Press

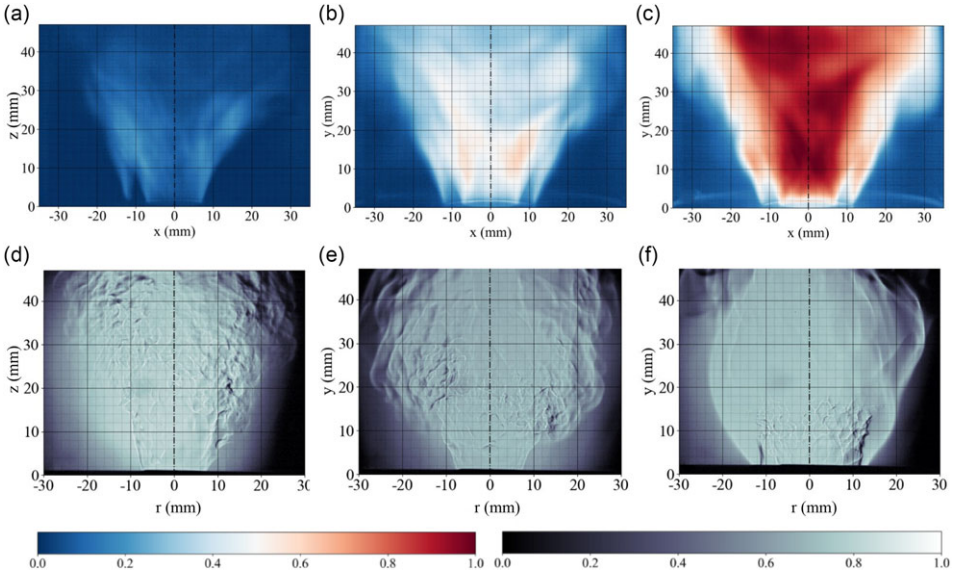

Figure 9. *Instantaneous chemiluminescence flame and shadowgraphs images for equivalence ratio 0.3 (left), 0.4 (center), and 0.5 (right) at constant air bulk velocity of 6 m* s^{-1} *are depicted.*

inner flame branch position is weakly affected by the operating condition because the swirl level is constant, one observes the regions of maximum heat release unsteadiness shifting downstream the swirling jets as the equivalence ratio increases. The instantaneous flame images are shown in Fig. 9(a–c) for each equivalence ratio. Thirdly, from the shadowgraphs in Fig. 9(d–f), one can distinguish instantaneous features such as the flame front reaction zones regions and turbulence induced flame wrinkling, without delineating though the preferential diffusion role. A shift from 'V' to 'M' flame is observed between equivalence ratio 0.4 in Fig. 9(e) and 0.5 in Fig. 9(f). This flame shape change is occurring at a different equivalence ratio compared to the chemiluminescence data because of the absence of the quartz tube when employing the shadowgraph technique. The 'M' flame length is considerably reduced compared to the 'V' flame. This feature is attributed to the addition of the outer branch in that case to compensate for the flame surface area modification.

The extraction of profiles of time-averaged, minimum and maximum chemiluminescence intensity downstream the bluff-body is documented in Fig. 10(a–c). These profiles show the line-of-sight integrated intensities and inform on the variations amplitudes in absolute values around the mean. The minimum and maximum values of the profile are taken as the minimum and maximum intensities at a given location (all r and $z = 13$ mm) for the entire time sequence. As the equivalence ratio is increased, the amplitude increases as well as the difference between maximum and minimum levels. This is observed for example on the centerline ($r = 0$). The variances computed are documented as profiles in Fig. 11(a–c). These profiles qualitatively indicate the level of unsteadiness of the flame and confirms this trend as the variance is increased overall at high equivalence ratio. The variance peaks in the outer flame branch for all cases. It is worth pointing out that the variance level taken at this one diameter length corresponds to the lower levels regions compared to other locations as seen in Fig. 8(d_1,e_1,f_1). These are important observations for the model developed and presented next. Indeed, the steady (coined static in Ref. (67)) and time-averaged flame fields can be assumed similar if the unsteadiness levels are low such as in the present case (see Ref. (38) for analytical comparison steady vs time-averaged). Accordingly, the flame angle processed from the time-averaged can be compared to the steady flame angle.

https://doi.org/10.1017/aer.2025.6 Published online by Cambridge University Press

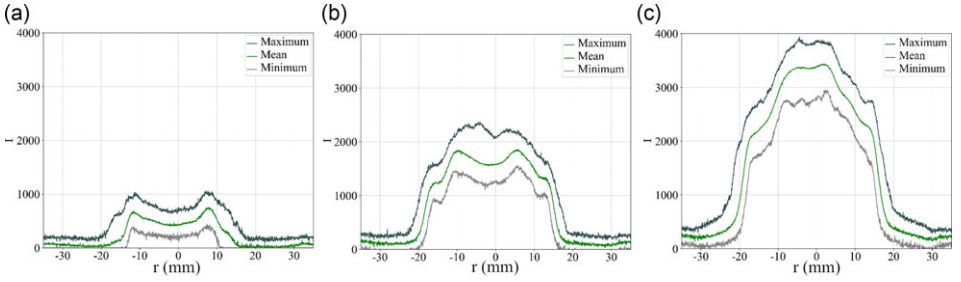

Figure 10. *Profiles of time-averaged, minimum and maximum chemiluminescence intensity extracted downstream the bluff-body.*

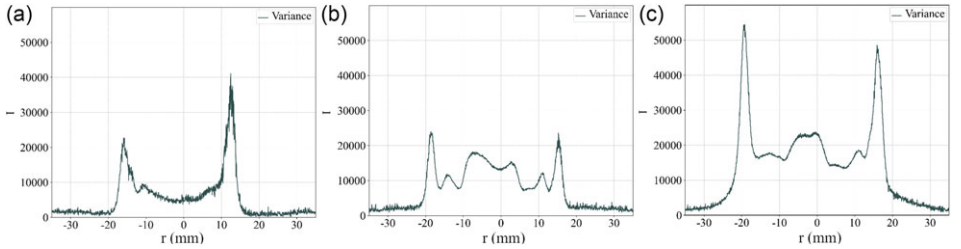

Figure 11. *Profiles of variance of chemiluminescence intensity extracted at one bluff-body diameter downstream the bluff-body.*

5.0 Theory for highly swirled lean fully premixed flame stabilisation

The demonstrations made and reported in the previous section have been driven by recent theoretical results indicating that premixed flame front stabilisation can be analysed with steady, unsteady, and instantaneous budgets [67] of the kinematic flame front condition [68]. This condition is defined as the balance between the flame surface vector $\mathbf{w}_s$, the flow velocity vector $\mathbf{v}$ and the local flame displacement speed S_d along the flame front normal vector $\mathbf{n}$. It is expressed as:

$$\mathbf{w}_s = \mathbf{v} + S_d\mathbf{n} \tag{8}$$

A concise stabilisation expression is obtained with the steady budget for this kinematic condition that results in:

$$v_{r,0}^2 + v_{\theta,0}^2 + v_{z,0}^2 = S_{d,0}^2 \tag{9}$$

where $v_{r,0}$, $v_{\theta,0}$, and $v_{z,0}$ are the local radial, azimuthal and axial steady velocity components whereas $S_{d,0}$ is the local flame displacement speed. In reacting swirling flows, at the interface of the inner recirculation zone and the swirling jets, by definition, there is a low, nearly zero velocity region where the left-hand side of this expression matches the local flame displacement speed. Based on this observation, this expression was developed and explored to lead to stabilisation of fully premixed hydrogen-air highly swirled flames. The criterion, noted Δ_s, is derived from the above expression. An azimuthal velocity scaling through a swirl velocity ratio is firstly introduced:

$$S = v_{\theta,0}/v_{z,0} \tag{10}$$

The swirl velocity ratio selected value is a trade-off between the geometrical swirl number defined based on geometry, see the calculation corresponding to Fig. 3(a) in Section 2 and Equation (1), and the condition imposed by Equation (13). A value of 0.74 is selected for S. A radial velocity scaling through

https://doi.org/10.1017/aer.2025.6 Published online by Cambridge University Press

the flame angle α as defined between the vertical axis and the local flame front surface is utilised as well:

$$\tan\alpha = v_{r,0}/v_{z,0} \tag{11}$$

This angle is obtained at the bluff-body tip assuming that the swirling jet drives the flame angle. Combining Equations (9), (10) and (11) leads to the concise criterion:

$$\Delta_s = v_{z,0}^2\left(\tan^2\alpha + S^2 + 1\right) - S_{d,0}^2 \tag{12}$$

Whereas the normal vector $\mathbf{n}_0$ of the steady flame front is perpendicular to the steady azimuthal velocity component $v_{\theta,0}\mathbf{e}_\theta$, the velocity $v_{\theta,0}$ is not zero. Additionally, the radial velocity ratio can be expressed as:

$$\tan\alpha = v_{r,0}/v_{z,0} = S/\beta\sqrt{1-\beta^2-(\beta/S)^2} \tag{13}$$

where the parameter $\beta = 0.57$ is the ratio of azimuthal velocity component to the local flame speed [67].

The stabilisation criterion Δ_s defined by Equation (12), requires: a steady axial velocity radial profile $v_{z,0}(r)$ at the bluff-body tip, and the stretched flame speed $S_{d,0}$. These are defined and documented next.

Firstly, the profile of steady axial velocity $v_{z,0}(r)$ (see Appendix A) is defined with:

$$v_{z,0}(r) = \frac{3}{2}U_b\left[1-\left(\frac{2r-r_o-r_i}{r_o-r_i}\right)^2\right] \tag{14}$$

Secondly, the stretched flame speed data are obtained as follows. In a first step, the flame stretch is derived analytically for the steady flame. The flame stretch κ [68, 69] of an elemental flame front surface area is defined as:

$$\kappa = \mathbf{nn}{:}\nabla\mathbf{v} + \nabla\cdot\mathbf{v} + S_d\nabla\cdot\mathbf{n} \tag{15}$$

Equation (15) includes three distinct terms: the flow strain at the flame front, the flow dilatation at the flame front, and the flame front curvature term. Accordingly, the explicit formulae of the flame stretch in cylindrical coordinates for the present flame can be derived. Neglecting the axial velocity gradient $\partial v_z/\partial z$ in the obtained flame stretch expression, assuming symmetry in the azimuthal direction of the steady flow $\partial/\partial\theta = 0$, and because the azimuthal normal steady flame front vector component $n_{\theta,0}$ is zero, the derivation in cylindrical coordinates yields to:

$$\kappa = \frac{\partial v_{z,0}}{\partial r}\cos\alpha\left[\sin\alpha - A_\alpha\cos\alpha\right] + \frac{A_\alpha}{r}\frac{\partial}{\partial r}\left(rv_{z,0}\right) + \cos\alpha\frac{S_L^0}{r} \tag{16}$$

The first term, associated with the flow strain cancels out because A_α is equal to $\tan\alpha$ as the radial and axial velocity components are linked with:

$$v_{r,0}(r) = A_\alpha v_{z,0}(r) \tag{17}$$

The second term due to the flow dilation, associated to local flow divergence, is neglected here because the flame stretch is evaluated on the unburnt gases side where the density is constant. The third expression represents the curvature of the steady highly swirled flame front. This expression of the flame stretch κ, Equation (16), is computed prior to determining the stretched laminar flame displacement speeds discussed now. The second step consists of computing the stretched flame speed $S_{d,0}$.

The stretched laminar flame displacement speed quantity S_L is identical to $S_{d,0}$ in the criterion Δ_s of Equation (12). It is worth pointing out that the steady flame front is laminar in nature here and thus the equality holds between S_L and $S_{d,0}$. The flame speed S_L is calculated considering a linear dependency on the flame stretch κ for the steady flow considered here. The unburnt stretched laminar flame speed is expressed as a function of the burnt gases Markstein length $\mathcal{L}_b$ [22] with:

$$S_L = S_L^0 - \mathcal{L}_b\kappa\frac{\rho_b}{\rho_u} \tag{18}$$

https://doi.org/10.1017/aer.2025.6 Published online by Cambridge University Press

Where ρ_u and ρ_b are the unburnt and burnt gas densities. The modified linear curvature model from Shu *et al.* [23] is used to get the stretched flame speed in this study. The Markstein length $\mathcal{L}_b$ is computed with the definition [23]:

$$\mathcal{L}_b = \delta_{th}\left[\frac{1}{Le} + \frac{Ze}{2}\left(1 - \frac{1}{Le}\right)\right] \tag{19}$$

Where the thermal flame thickness is defined following Sun *et al.* [70]:

$$\delta_{th} = \frac{T_b - T_u}{|\nabla T|_{max}} \tag{20}$$

The Lewis number Le is defined as the ratio of thermal diffusivity and mixture-averaged hydrogen species diffusion coefficient [71]. The Zeldovitch number is defined [23] with:

$$Ze = 4\frac{T_b - T_u}{T_b - T^0} \tag{21}$$

where T^0 is the inner flame temperature corresponding to the highest heat release location in the flame front. This temperature is computed with:

$$T_0 = T_u + 0.7\,(T_b - T_u) \tag{22}$$

where 0.7 is the non-dimensional temperature value used for identification of the reaction zone. In addition to the Markstein lengths and the flame stretch in Equation (18), the unstretched S_L^0 laminar flame displacement speeds were next extracted from experimental and chemical kinetic literature data, see Appendix B. Inserting the above expressions with the Markstein length Equation (19) yields the unburnt side stretched laminar flame displacements speeds S_L in Equation (18) for each equivalence ratio ranging from 0.3 to unity.

All quantities computed to calculate the criterion Δ_s are taken on the unburnt side of the flame (stretched flame speed, non-dimensional numbers, transport and thermodynamics data, Markstein lengths, and parabolic velocity profile) so that the constant density flow (non-reacting) assumption is valid. This ensures consistency throughout the data and models taken from literature or derived here. The same approach is taken in von Elbe and Lewis [30] or in Cheng *et al.* [32]. The criterion Δ_s can be assessed at any points of the flame surface. Its application to the bluff-body tip location where the wall no-slip condition induces the lowest flow speeds is particularly of interest because the flame front can propagate through flashback [16, 53]. In this near wall region, it is known that a strong heat transfer occurs from the flame to the walls inducing local extinction. The minimum distance between the wall (the bluff-body here) and the flame front location (defined by its maximum chemical heat release) is known as the quenching distance over which a flame front cannot propagate because the wall induces a cooling effect on the flame. This quenching distance must thus be considered to include the flashback propensity in the criterion Δ_s.

There are two distinct set of research in literature focusing on quenching distances: (i) studies focusing on wall boundary layer flashback, and (ii) studies focusing on flame-wall interactions. In the former, the flame quenching distance and the critical velocity gradient in the boundary layer are at work [8, 30, 55] to balance the local flame speed and the local axial flow speed. In the latter, a Peclet number $\mathrm{Pe}_Q = y_Q/\delta = y_Q/\delta$ is introduced to define the quenching distance y_Q for a given flame-wall interaction [8, 72, 73] with respect to the thermal laminar flame thickness δ. Several configurations have been studied in the literature indicating that the Peclet number can vary from 0.38 [74] to 1.4 [75] on head-on quenching, and up to 3 on side-wall quenching [73] for hydrogen/air premixed flames. A value of unity leads to matching both research areas conditions and it is selected here so that $\mathrm{Pe}_Q = 1$. The thermal diffusive flame thickness $\delta = \lambda/\left(\rho c_p S_L^0\right)$ in quiet mixture [76, 77] is introduced and used, and the criterion Δ_s is assessed at a radius equal to the quenching distance. The quantity Δ_s is assessed carefully and compared to experimental measurements obtained from the experiment in the next section.

In Fig. 12, all the notations including vectors, flame angle α, quenching distance y_Q, relevant to the kinematic description are depicted.

https://doi.org/10.1017/aer.2025.6 Published online by Cambridge University Press

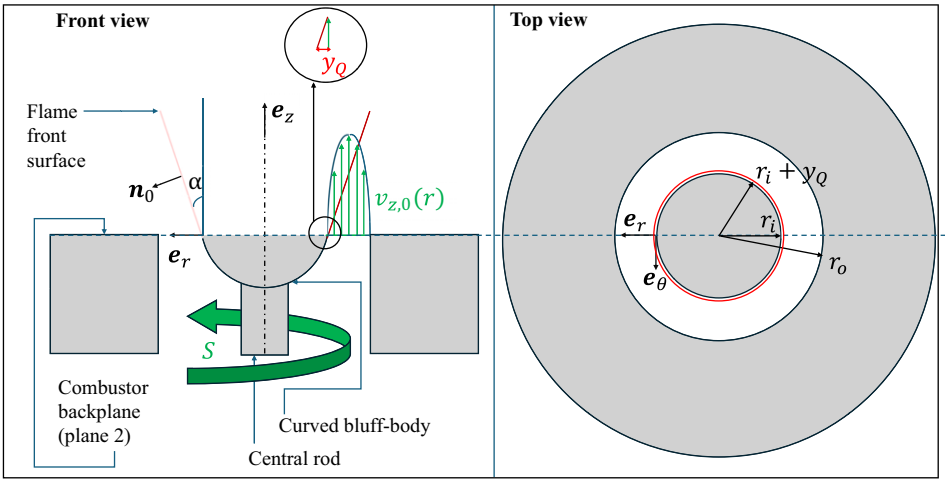

Figure 12. *Premixed swirling flame stabilisation kinematic descriptive schematic.*

6.0 Comparison between theory versus experimental data: results and regimes

Experimental measurements are reported in Fig. 13 as symbols on a colourmap that represents the value of the criterion Δ_s defined by Equation (12), with the Conaire *et al.* chemical kinetic mechanism [63]. The inlet temperature is 295 K and the operating pressure is one atmosphere. A value of zero for Δ_s indicates an equal balance between squared steady flame front speed and flow velocity terms when the steady flame surface speed $\mathbf{w}_0^s$ is zero. A positive value of Δ_s indicates that the flame front surface is propagating downstream, and a negative value indicates it is propagating upstream. This latter case is directly associated with flashback as the criterion is evaluated along the radius at a height located at the tip of the bluff-body. The natural blowout and blowoff data were not characterised in the present study as the minimum equivalence ratio investigated was 0.3, which is above the lean flammability limit. Yet, the proposed criterion is valid, and a particular value of that criterion may exist for blowoff/blowout when reached. This will require an instantaneous quantitative study of the kinematic budget. The superimposed grid (x and y directions) in Fig. 13 represents the uncertainty range associated with laminar flame speed measurement introduced in previous section. The grey line represents the swirled flame solution line.

The premixed swirling flame stabilisation map plotted in Fig. 13 enables to distinguish key regimes and their boundaries:

1. Flashbacked flame regime as $\Delta_s < 0$.
2. Stabilised flame regime as $\Delta_s > 0$.
3. Stabilisation criterion line $\Delta_s = 0$.
4. Swirled flame solution line $\tau_{cv}/\tau_b = 1$.

The swirled flame solution line is defined as the ratio of the characteristic flame convective time τ_{cv} that is equal to $\delta/\left[2/3v_{z,0}\right]$ to the flame propagation characteristic time τ_b defined with δ/S_d. This line results from the kinematic flame front condition estimated with its instantaneous budget form. When this ratio is below unity, it is expected that no flame can be sustained on the burner where the flow velocity profile is imposed, unlike when this ratio is above unity. This line is in the region where $\Delta_s < 0$ for the present case. In other words, the flashback region overlaps and encompasses this line.

It is striking to observe how the stabilisation criterion lines (red, white, cyan) in Fig. 13 delineate the experimental flashback (red dots) and stabilised flame points (green dots and blue triangles) within the uncertainty range defined as the superimposed grid. The criterion lines (red and white) follow the trend

https://doi.org/10.1017/aer.2025.6 Published online by Cambridge University Press

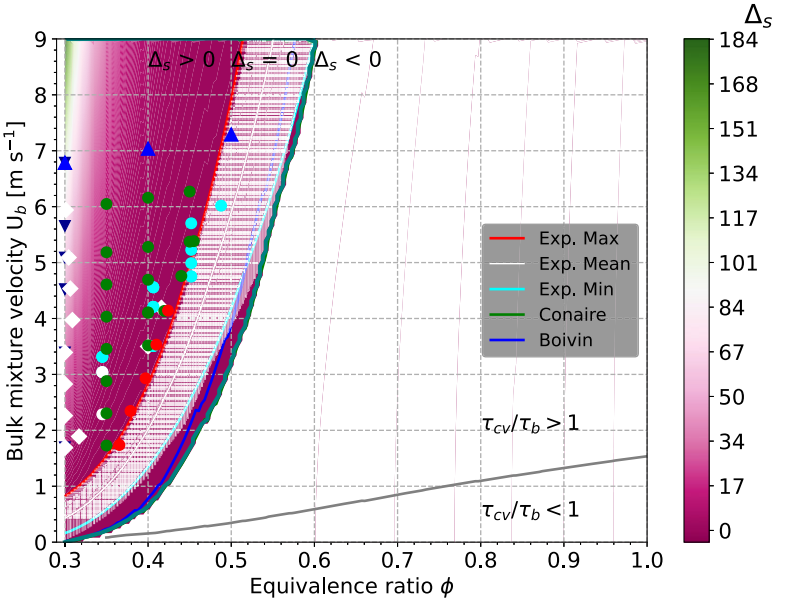

Figure 13. *Premixed swirling flame stabilisation map. The criterion value Δ_s map is represented as a function of the equivalence ratio ϕ and the inlet bulk mixture axial velocity U_b. Symbols represent experimental data points. Experimental ignition points (white squares), flashback (red dots) and stabilised flame points (green, cyan dots, blue triangles-down and triangles-up) are superimposed. Red, white and cyan curves correspond to isolines of the criterion $\Delta_s = 0$ made with experimental flame speed data (maximum, mean and minimum values of S_L^0 taken from Han et al.) whereas green and blue curves correspond to chemical kinetic models.*

of the experimental data and the theoretical values agree within the range of uncertainties defined in the previous section and it is thus considered to be satisfactory. At an equivalence ratio ϕ of 0.5 and a bulk flow velocity of 6 m s^{-1}, the range varies between 0.45 and 0.55, which corresponds to $\pm 10\%$ variation of 0.5. Whereas the theoretical predictions made are based on the steady kinematic condition and the experiments include all unsteady processes at work, the criterion delineates well the stabilised regime.

7.0 Conclusion

This article presents an experiment that demonstrated, experimentally and for the first time, combustion in the fully lean premixed highly swirled turbulent regime for hydrogen-air mixtures. A mechanistic model for flame stabilisation is presented and validated with the experimental data points obtained. The model relies on the steady form of the kinematic balance between the flame and the flow taking into account the three-dimensionality of the swirling flowfield (all velocity components). The role of the quenching distance at the bluff-body tip is folded into the model. This model delineates the region of flashback versus the stabilised flames region. The uncertainty about the unstretched laminar flame displacement speed dominates the total theoretical model uncertainty in this study. The perspectives of this research work include assessing the scalability of highly swirled lean fully premixed H_2/Air flames to industrial configurations and operating conditions along with detailed quantitative analysis of the instantaneous kinematic budget. The associated challenges for this scaling can be associated with three groups of parameters: (1) the flow and flame conditions (inlet temperature, density and operating pressure) modified between atmospheric laboratory scale and engine relevant operation impacting the quenching distance y_Q significantly; (2) the flame speed S_L value and the axial flow speed profile along the radius $v_{z,0}$ (r) impacting the value of Δ_s; and (3) the mode of stabilisation that is presently supported

https://doi.org/10.1017/aer.2025.6 Published online by Cambridge University Press

by steady flow-flame kinematic budget but can be driven by the unsteady budget too. Parametric studies at preheated and high-pressure plus high-temperature conditions could be conducted in future work. The experiment described, the measurements conducted, and the theoretical model developed in this article can contribute to achieve future zero-carbon and low nitrogen oxides emission aviation based on hydrogen combustion.

Competing interests. The authors declare none.

Acknowledgments. Technical support for the project on design and operation by Sagar Godse, Jonathan Kolwyck, Joel Davenport and Larry Alexander is sincerely acknowledged. The authors would also like to thank Sunil Patil and Carlo Arguinzoni for the computational data.

References

[1] National Research Council, Division on Engineering, Physical Sciences, Board on Energy, Environmental Systems, Committee on Alternatives, and Strategies for Future Hydrogen Production. *The hydrogen economy: opportunities, costs, barriers, and research and development needs*. National Academies Press, 2004.
[2] Zeldovich, Y.B. The oxidation of nitrogen in combustion and explosions, *J. Acta Physicochimica*, 1946, **21**, p 577.
[3] Beér, J.M. and Chigier, N.A. *Combustion aerodynamics*. Applied Science Publishers Ltd, 1972.
[4] Gupta, A.K. Swirl flows, 1984.
[5] Karagozian, A. Frank Marble, 1918–2014: Tribute to an aerospace giant, *Proc. Nat. Acad. Sci.*, 2015, **112**, (18), pp 5550–5551.
[6] Zukoski, E.E. and Marble, F.E. Experiments concerning the mechanism of flame blowoff from bluff bodies, In *Proceedings of the Gas Dynamics Symposium on Aerothermochemistry*, pages 205–210. Northwestern University Press, 1956.
[7] Ballal, D.R. and Lefebvre, A.H. The structure and propagation of turbulent flames, *Proc. Royal Soc. London A Math. Phys. Sci.*, 1975, **344**, (1637), pp 217–234.
[8] Kalantari, A. and McDonell, V. Boundary layer flashback of non-swirling premixed flames: Mechanisms, fundamental research, and recent advances, *Prog. Energy Combust. Sci.*, 2017, **61**, pp 249–292.
[9] Shanbhogue, S.J., Husain, S. and Lieuwen, T. Lean blowoff of bluff body stabilized flames: Scaling and dynamics, *Prog. Energy Combust. Sci.*, **35**(1):98–120, 2009.
[10] Sarpkaya, T. Vortex breakdown in swirling conical flows, *AIAA J.*, 1971, **9**, (9), pp 1792–1799.
[11] Sarpkaya, T. On stationary and travelling vortex breakdowns, *J Fluid Mech*, 1971, **45**, (3), pp 545–559.
[12] O'Connor, J. Visualization of shear layer dynamics in a transversely forced flow and flame, *J Propul Power*, 2015, **31**, (4), 1127–1136.
[13] Oberleithner, K., Sieber, M., Nayeri, C.N., Paschereit, C.O., Petz, C., Hege, H.-C., Noack, B.R. and Wygnanski, I. Three-dimensional coherent structures in a swirling jet undergoing vortex breakdown: stability analysis and empirical mode construction, *J. Fluid Mech.*, 2011, **679**, pp 383–414.
[14] Syred, N. A review of oscillation mechanisms and the role of the precessing vortex core (pvc) in swirl combustion systems, *Prog. Energy Combust. Sci.*, 2006, **32**, (2), pp 93–161.
[15] An, Q., Kwong, W.Y., Geraedts, B.D. and Steinberg, A.M. Coupled dynamics of lift-off and precessing vortex core formation in swirl flames, *Combust Flame*, 2016, **168**, pp 228–239.
[16] Novoselov, A.G., Ebi, D. and Noiray, N. Confined boundary-layer flashback flame dynamics in a turbulent swirling flow. *AIAA J.*, 2023, **61**, (4), pp 1548–1554.
[17] Veynante, D. and Vervisch, L. Turbulent combustion modeling, *Prog. Energy Combust. Sci.*, 2002, **28**, (3), pp 193–266.
[18] Veynante, D. Investigation of flame surface density modeling for large eddy simulation of turbulent premixed flames by comparison with a prescribed reference solution, *Combust Flame*, 2022, **239**, p 111663.
[19] Giannakopoulos, G.K., Gatzoulis, A., Frouzakis, C.E., Matalon, M. and Tomboulides, A.G. Consistent definitions of "flame displacement speed" and "Markstein length" for premixed flame propagation. *Combust Flame*, 2015, **162**, (4), pp 1249–1264.
[20] Driscoll, J.F. Turbulent premixed combustion: Flamelet structure and its effect on turbulent burning velocities. *Prog Energy Combust Sci*, **34**(1):91–134, 2008.
[21] Chen, J.B. and Im, H.G. Stretch effects on the burning velocity of turbulent premixed hydrogen/air flames, *Proc. Combust. Inst.*, 2000, **28**, (1), pp 211–218.
[22] Beeckmann, J., Hesse, R., Kruse, S., Berens, A., Peters, N., Pitsch, H. and Matalon, M. Propagation speed and stability of spherically expanding hydrogen/air flames: Experimental study and asymptotics, *Proc. Combust. Inst.*, 2017, **36**, (1), pp 1531–1538.
[23] Shu, T., Xue, Y., Liang, W. and Ren, Z. Extrapolations of laminar flame speeds from expanding spherical flames based on the finite-structure stretched flames, *Combust Flame*, 2021, **226**, pp 445–454.
[24] Wang, S., Elbaz, A.M., Wang, G., Wang, Z. and Roberts, W.L. Turbulent flame speed of -NH_3/-CH_4/-H_2/-H_2O/air-mixtures: Effects of elevated pressure and Lewis number, *Combust Flame*, 2023, **247**, p 112488.

https://doi.org/10.1017/aer.2025.6 Published online by Cambridge University Press

[25] Day, M., Tachibana, S., Bell, J., Lijewski, M., Beckner, V. and Cheng, R.K. A combined computational and experimental characterization of lean premixed turbulent low swirl laboratory flames II. Hydrogen flames, *Combust Flame*, 2015, **162**, (5), pp 2148–2165.

[26] Bell, J.B., Cheng, R.K., Day, M.S., Beckner, V.E. and Lijewski, M.J. Interaction of turblence and chemistry in a low-swirl burner, In *Journal of Physics: Conference Series*, vol. 125, p 012027. IOP Publishing, 2008.

[27] Aspden, A.J., Day, M.S. and Bell, J.B. Turbulence–flame interactions in lean premixed hydrogen: transition to the distributed burning regime, *J. Fluid Mech.*, 2011, **680**, pp 287–320.

[28] Grcar, J.F., Bell, J.B. and Day, M.S. The soret effect in naturally propagating, premixed, lean, hydrogen–air flames, *Proc. Combust. Inst.*, 2009, **32**, (1), pp 1173–1180.

[29] Xiao, G. and Palies, P. Towards scales resolving direct simulation of a hydrogen/air lean premixed flame with Swirler-induced turbulence, In *Turbo Expo: Power for Land, Sea, and Air*, vol. 86960, p V03BT04A033. American Society of Mechanical Engineers, 2023.

[30] Von Elbe, G. and Lewis, B. Theory of ignition, quenching and stabilization of flames of nonturbulent gas mixtures, In *Symposium on Combustion and Flame, and Explosion Phenomena*, vol. 3, pp 68–79. Elsevier, 1948.

[31] Yegian, D.T. and Cheng, R.K. Development of a lean premixed low-swirl burner for low -NO_x practical applications. *Combust. Sci. Technol.*, 1998, **139**, (1), pp 207–227.

[32] Cheng, R.K., Littlejohn, D., Strakey, P.A. and Sidwell, T. Laboratory investigations of a low-swirl injector with -H_2 and -CH_4 at gas turbine conditions, *Proc. Combust. Inst.*, 2009, **32**, (2), pp 3001–3009.

[33] Williams, T.C., Schefer, R.W., Oefelein, J.C. and Shaddix, C.R. Idealized gas turbine combustor for performance research and validation of large eddy simulations. *Rev. Sci. Instrum.*, 2007, **78**, (3), p 035114.

[34] Thumuluru, S.K. and Lieuwen, T. Characterization of acoustically forced swirl flame dynamics, *Proc. Combust. Inst.*, 2009, **32**, (2), pp 2893–2900.

[35] Palies, P., Durox, D., Schuller, T., Morenton, P. and Candel, S. Dynamics of premixed confined swirling flames. *CR Mec.*, 2009, **337**, (6–7), pp 395–405.

[36] Davis, D.W., Therkelsen, P.L., Littlejohn, D. and Cheng, R.K. Effects of hydrogen on the thermo-acoustics coupling mechanisms of low-swirl injector flames in a model gas turbine combustor, *Proc. Combust. Inst.*, 2013, **34**, (2), pp 3135–3143.

[37] Therkelsen, P.L., Portillo, J.E., Littlejohn, D., Martin, S.M. and Cheng, R.K. Self-induced unstable behaviors of -CH_4 and -H_2/-CH_4 flames in a model combustor with a low-swirl injector. *Combust. Flame*, 2013, **160**, (2), pp 307–321.

[38] Palies, P., Ilak, M. and Cheng, R. Transient and limit cycle combustion dynamics analysis of turbulent premixed swirling flames, *J. Fluid Mech.*, 2017, **830**, pp 681–707.

[39] Schefer, R.W., Wicksall, D.M. and Agrawal, A.K. Combustion of hydrogen-enriched methane in a lean premixed swirl-stabilized burner, *Proc. Combust. Inst.*, 2002, **29**, (1), pp 843–851.

[40] Burguburu, J., Cabot, G., Renou, B., Boukhalfa, A.M. and Cazalens, M. Effects of -H_2 enrichment on flame stability and pollutant emissions for a kerosene/air swirled flame with an aeronautical fuel injector, *Proc. Combust. Inst.*, 2011, **33**, (2), pp 2927–2935.

[41] Taamallah, S., Shanbhogue, S.J. and Ghoniem, A.F. Turbulent flame stabilization modes in premixed swirl combustion: Physical mechanism and Karlovitz number-based criterion. *Combust. Flame*, 2016, **166**, pp 19–33.

[42] Guiberti, T.F., Durox, D., Scouflaire, P. and Schuller, T. Impact of heat loss and hydrogen enrichment on the shape of confined swirling flames, Proc. Combust. Inst., 2015, 35, (2), pp 1385–1392.

[43] Chterev, I. and Boxx, I. Effect of hydrogen enrichment on the dynamics of a lean technically premixed elevated pressure flame, *Combust. Flame*, 2021, **225**, pp 149–159.

[44] Agostinelli, P.W., Laera, D., Chterev, I., Boxx, I., Gicquel, L. and Poinsot, T. Large eddy simulations of mean pressure and -H_2 addition effects on the stabilization and dynamics of a partially-premixed swirled-stabilized methane flame, *Combust. Flame*, 2023, **249**, p 112592.

[45] Reichel, T.G., Terhaar, S. and Paschereit, O. Increasing flashback resistance in lean premixed swirl-stabilized hydrogen combustion by axial air injection, *J. Eng. Gas Turbines Power*, 2015, **137**, (7), p 071503.

[46] Reichel, T.G., Goeckeler, K. and Paschereit, O. Investigation of lean premixed swirl-stabilized hydrogen burner with axial air injection using OH-PLIF imaging, *J. Eng. Gas Turbines Power*, 2015, **137**, (11), p 111513.

[47] Sattelmayer, T., Mayer, C. and Sangl, J. Interaction of flame flashback mechanisms in premixed hydrogen-air swirl flames, *J. Eng. Gas Turbines Power*, 2016, **138**, (1), p 011503.

[48] Mayer, C., Sangl, J., Sattelmayer, T., Lachaux, T. and Bernero, S. Study on the operational window of a swirl stabilized syngas burner under atmospheric and high pressure conditions, *J. Eng. Gas Turbines Power*, 2012, **134**, (3), p 031506.

[49] Palies, P. and Acharya, R. Flame-resolved transient simulation with swirler-induced turbulence applied to lean blowoff premixed flame experiment, *Combust. Flame*, 2021, **226**, pp 14–30.

[50] Chowdhury, B.R. and Cetegen, B.M. Effects of free stream flow turbulence on blowoff characteristics of bluff-body stabilized premixed flames, *Combust. Flame*, 2018, **190**, pp 302–316.

[51] Kumar, R.M., Chterev, I., Stepien, D., Sirignano, M., Emerson, B.L., Fugger, C.A., Jiang, N., Roy, S. and Lieuwen, T.C. Near blowout dynamics of a premixed, swirl stabilized flame, *Proc. Combust. Inst.*, 2021, **38**, (4), pp 6067–6075.

[52] Cavaliere, D.E., Kariuki, J. and Mastorakos, E. A comparison of the blow-off behaviour of swirl-stabilized premixed, non-premixed and spray flames, *Flow Turbul. Combust.*, 2013, **91**, pp 347–372.

[53] Ebi, D. and Clemens, N.T. Experimental investigation of upstream flame propagation during boundary layer flashback of swirl flames, *Combust. Flame*, 2016, **168**, pp 39–52.

https://doi.org/10.1017/aer.2025.6 Published online by Cambridge University Press

[54] Ranjan, R., Ebi, D.F. and Clemens, N.T. Role of inertial forces in flame-flow interaction during premixed swirl flame flashback, Proc. Combust. Inst., 2019, 37, (4), pp 5155–5162.
[55] Novoselov, A.G., Ebi, D. and Noiray, N. Accurate prediction of confined turbulent boundary layer flashback through a critically strained flame model, *J. Eng. Gas Turbines Power*, 2022, **144**, (10), p 101013.
[56] Hong, S.-W. and Song, J.-H. Flame-quenching model of the quenching mesh for H_2-air mixtures, *J. Nucl. Sci. Technol.*, 2013, **50**, (12), pp 1213–1219.
[57] Caulfield, C.J., Patil, S., Arguinzoni, C., Ansari, N. and Palies, P. Initial numerical simulations of a laboratory-scale premixed hydrogen/air high swirl experiment. In *Turbo Expo: Power for Land, Sea, and Air*, vol. 86953, p V03AT04A029. American Society of Mechanical Engineers, 2023.
[58] Palies, P. *Dynamique et instabilités de combustion des flammes swirlées*. PhD thesis, Ecole Centrale Paris, 2010.
[59] Palies, P., Schuller, T., Durox, D., Gicquel, L.Y.M. and Candel, S. Acoustically perturbed turbulent premixed swirling flames, *Phys. Fluids*, 2011, **23**, (3), p 037101.
[60] Goodwin, D.G., Speth, R.L., Moffat, H.K. and Weber, B.W. Cantera: An object-oriented software toolkit for chemical kinetics, thermodynamics, and transport processes, 2018.
[61] Palies, P. *Stabilization and Dynamic of Premixed Swirling Flames: Prevaporized, Stratified, Partially, and Fully Premixed Regimes*. Academic Press, 2020.
[62] Hickstein, D.D., Gibson, S.T., Yurchak, R., Das, D.D. and Ryazanov, M. A direct comparison of high-speed methods for the numerical Abel transform, *Rev. Sci. Instrum.*, 2019, **90**, (6), p 065115.
[63] Conaire, M.Ó., Curran, H.J., Simmie, J.M., Pitz, W.J. and Westbrook, C.K. A comprehensive modeling study of hydrogen oxidation, *Int. J. Chem. Kinet.*, 2004, **36**, (11), pp 603–622.
[64] Mao, R., Wang, J., Lin, W., Han, W., Zhang, W. and Huang, Z. Effects of flow–flame interactions on the stabilization of ultra-lean swirling -CH_4/H_2/Air flames, *Fuel*, 2022, **319**, p 123619.
[65] Stöhr, M., Oberleithner, K., Sieber, M., Yin, Z. and Meier, W. Experimental study of transient mechanisms of Bistable flame shape transitions in a swirl combustor, *J. Eng. Gas Turbines Power*, 2018, **140**, (1), p 011503.
[66] Guiberti, T.F., Zimmer, L., Durox, D. and Schuller, T. Experimental analysis of V-to M-shape transition of premixed CH_4/H_2/Air swirling flames, In *Turbo Expo: Power for Land, Sea, and Air*, vol. 55102, p V01AT04A063. American Society of Mechanical Engineers, 2013.
[67] Palies, P. The flame displacement speed: a key quantity for turbulent combustion and combustion instability, *Int. J. Spray Combust. Dyn.*, **14**(1-2):4–16, 2022.
[68] Candel, S.M. and Poinsot, T.J. Flame stretch and the balance equation for the flame area. *Combust. Sci. Technol.*, 1990, **70**(1–3), pp 1–15.
[69] Matalon, M. On flame stretch. *Combust. Sci. Technol.*, 1983, **31**(3–4), pp 169–181.
[70] Sun, C.J., Sung, C.-J., He, L. and Law, C.-K. Dynamics of weakly stretched flames: quantitative description and extraction of global flame parameters. *Combust Flame*, **118**(1-2):108–128, 1999.
[71] Chen, J.H., Choudhary, A., De Supinski, B., DeVries, M., Hawkes, E.R., Klasky, S., Liao, W.-K., Ma, K.-L., Mellor-Crummey, J. and Podhorszki, N. Terascale direct numerical simulations of turbulent combustion using S3D, *Comput. Sci. Discovery*, 2009, **2**, (1), p 015001.
[72] Poinsot, T.J., Haworth, D.C. and Bruneaux, G. Direct simulation and modeling of flame-wall interaction for premixed turbulent combustion. *Combust. Flame*, 1993, **95**(1-2), pp 118–132.
[73] Enomoto, M. Sidewall quenching of laminar premixed flames propagating along the single wall surface. *Proceedings of the Combustion Institute*, 29(1):781–787, 2002.
[74] Gruber, A., Sankaran, R., Hawkes, E.R. and Chen, J.H. Turbulent flame–wall interaction: a direct numerical simulation study, *J. Fluid Mech.*, 2010, **658**, pp 5–32.
[75] Lai, J., Ahmed, U., Klein, M. and Chakraborty, N. A comparison between head-on quenching of stoichiometric methane-air and hydrogen-air premixed flames using direct numerical simulations, *Int. J. Heat Fluid Flow*, 2022, **93**, p 108896.
[76] Ballal, D.R. and Lefebvre, A.H. Ignition and flame quenching in flowing gaseous mixtures, *Proc. Royal Soc. London A Math. Phys. Sci.*, 1977, **357**, (1689), pp 163–181.
[77] Williams, F.A. *Combustion Theory*. CRC Press, 2018.
[78] Lobasov, A.S., Alekseenko, S.V., Markovich, D.M. and Dulin, V.M. Mass and momentum transport in the near field of swirling turbulent jets. Effect of swirl rate, *Int. J. Heat Fluid Flow*, 2020, **83**, p 108539.
[79] Durox, D., Moeck, J.P., Bourgouin, J.-F., Morenton, P., Viallon, M., Schuller, T. and Candel, S. Flame dynamics of a variable swirl number system and instability control, *Combust Flame*, 2013, **160**, (9), pp 1729–1742.
[80] Palies, P., Durox, D., Schuller, T. and Candel, S. The combined dynamics of swirler and turbulent premixed swirling flames, *Combust Flame*, 2010, **157**, (9), pp 1698–1717.
[81] Boivin, P., Sánchez, A.L. and Williams, F.A. Explicit analytic prediction for hydrogen–oxygen ignition times at temperatures below crossover, *Combust. Flame*, 2012, **159**, (2), pp 748–752.
[82] Boivin, P. *Reduced-kinetic mechanisms for hydrogen and syngas combustion including autoignition*. PhD thesis, 2011.
[83] Han, W., Dai, P., Gou, X. and Chen, Z. A review of laminar flame speeds of hydrogen and syngas measured from propagating spherical flames, *Appl. Energy Combust. Sci.*, 2020, **1**, p 100008.

https://doi.org/10.1017/aer.2025.6 Published online by Cambridge University Press

Appendix

Appendix A. Velocity profile and CFD validation

The axial velocity $v_{z,0}\,(r)$ radial profile model derivation utilised for the criterion Equation (12) is outlined in this section. The derivation begins with the axial momentum governing equation expressed in cylindrical coordinates:

$$\frac{\partial v_z}{\partial t} + v_r \frac{\partial v_z}{\partial r} + \frac{v_\theta}{r}\frac{\partial v_z}{\partial \theta} + v_z \frac{\partial v_z}{\partial z} = -\frac{1}{\rho}\frac{\partial p}{\partial z} + \nu\left(\frac{1}{r}\frac{\partial}{\partial r}\left(r\frac{\partial v_z}{\partial r}\right) + \frac{1}{r^2}\frac{\partial^2 v_z}{\partial z^2}\right) - g \tag{A1}$$

Next, the flow inside the injector, from the outlet of the swirler to the bluff-body tip, is assumed steady and azimuthaly symmetric. Two additional assumptions are made: the axial flow velocity is dependent on the radius only and the radial velocity is of lower amplitude compared to the axial flow velocity and thus it is neglected. This yields to:

$$-\frac{1}{\rho}\frac{\partial p}{\partial z} = \frac{\nu}{r}\frac{\partial}{\partial r}\left(r\frac{\partial v_z}{\partial r}\right) \tag{A2}$$

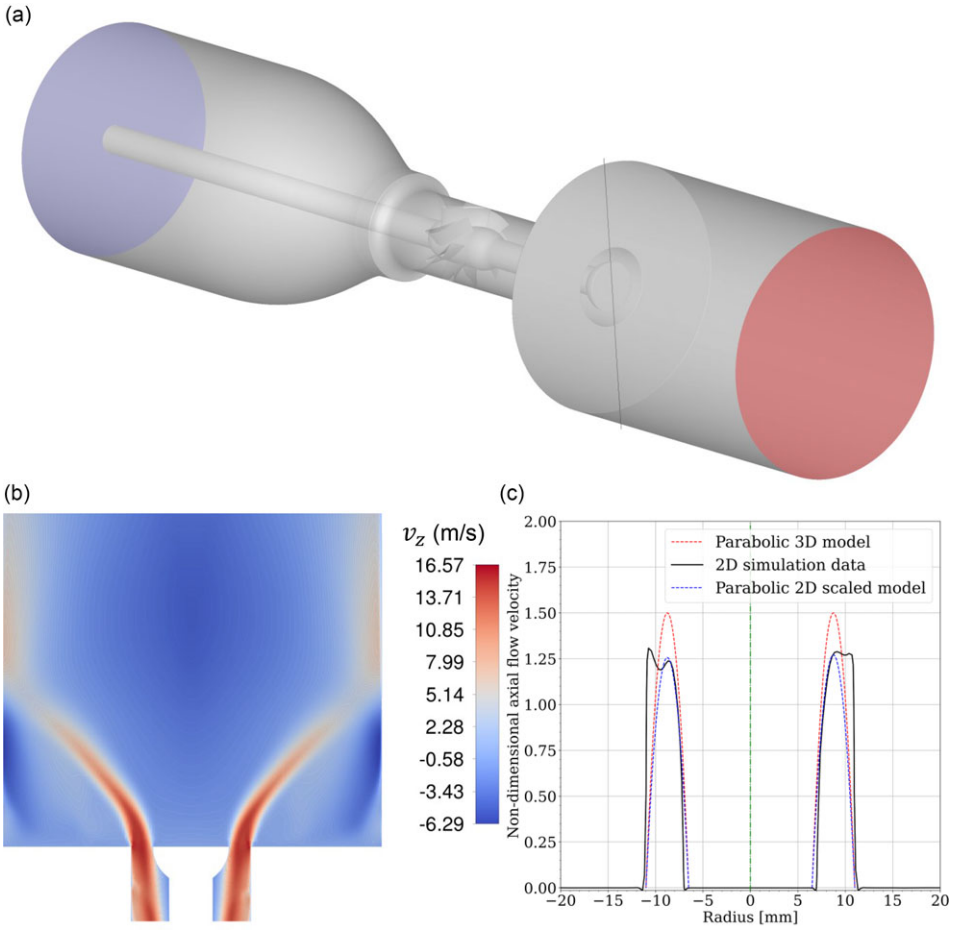

Figure A1. *Comparison between CFD data and modeled parabolic profile. (a) Isometric view of the computational domain with location of velocity profile extraction (vertical black line). (b) Cutplane of the time-averaged axial velocity field for U_b of 12 m s^{-1}. (c) Comparison of non-dimensional axial velocity profiles taken from computational data and parabolic model used in the present study.*

https://doi.org/10.1017/aer.2025.6 Published online by Cambridge University Press

Table A1. *Flame speed data. Experimental and chemical kinetic unstretched laminar flame displacement speeds data utilised in this study are listed. Data reported are function of the equivalence ratio ϕ and are expressed in m s^{-1}.*

Φ	Exp. min S_L^0 [83]	Exp. max S_L^0 [83]	Exp. mean S_L^0 [83]	Boivin [82]	Conaire [63]
0.3	0.05	0.17	0.11	0.04	0.02
0.4	0.30	0.40	0.35	0.19	0.17
0.5	0.42	0.65	0.53	0.48	0.44
0.6	0.80	1.02	0.91	0.84	1.09
0.7	1.05	1.45	1.25	1.20	1.40
0.8	1.30	1.80	1.55	1.54	1.69
0.9	1.70	1.95	1.82	1.85	1.98
1	1.95	2.27	2.11	2.11	2.00

Which is expressed as follows by expanding the right-hand side term:

$$-\frac{1}{\rho}\frac{\partial p}{\partial z} = \nu\left(\frac{1}{r}\frac{\partial v_z}{\partial r} + \frac{\partial v_z^2}{\partial r^2}\right) \tag{A3}$$

One observes that Equation (A3) is almost identical to the equation used for the classical derivation of the parabolic velocity profile in steady laminar pipe. Based on this observation, the solution proposed for the steady axial velocity $v_{z,0}\,(r)$ is:

$$v_{z,0}\,(r) = \frac{3}{2}U_b\left[1 - \left(\frac{2r - r_o - r_i}{r_o - r_i}\right)^2\right] \tag{A4}$$

The axial velocity radial profile Equation (A4) is adopted for the present work.

A comparison of the resulting profile with time-averaged non-dimensional numerical simulations data is documented in Fig. A1. Swirling flow axial velocity time-averaged profiles experimentally measured in literature indicate a parabolic dependency as well as a function of the radius [78–80]. Acknowledging the differences between the steady and the time-averaged fields, such observations support the use of a parabolic profile here.

Appendix B. Unstretched laminar flame speed data

The unstretched flame speeds calculations required to evaluate the stretched laminar flame speeds in Equation (12) are now documented. The quantity S_L^0 is first computed based on literature chemical kinetic data by Boivin *et al.* and Conaire *et al.* [63, 81, 82] as well as experimental data from Han *et al.* [83]. Table A1 lists the laminar flame displacement speeds S_L^0 computed with these two chemical kinetic mechanisms and those measured experimentally [83].

The computed flame speed data are extracted from one-dimensional hydrogen-air premixed flame simulations conducted with the open-source chemical kinetic software cantera [60] with multicomponent transport, Soret and Dufour effects taken into account. The experimental data minimum and maximum values (corresponding to columns 2 and 3 of Table A1) for each equivalence ratio are used to determine uncertainty ranges.

Cite this article: Palies P. and Premchand C.P. (2025). Hydrogen-air lean premixed turbulent highly swirled flames stabilisation: experimental demonstration and mechanistic-kinematic description. *The Aeronautical Journal*, **129**, 1421–1444. https://doi.org/10.1017/aer.2025.6